buildings

MDPI

Article

Physics-Informed Active Learning for Calibrating Mesoscopic Dynamic Parameters of Multiphase Concrete in DEM Simulations

Jinyuan Huang [1], Zhongyuan Li [1] and Tingting Zhao [1,2,*]

[1] College of Aeronautics and Astronautics, Taiyuan University of Technology, Taiyuan 030024, China
[2] Shanxi Key Laboratory of Material Strength & Structural Impact, Taiyuan University of Technology, Taiyuan 030024, China
* Correspondence: zhaotingting@tyut.edu.cn; Tel.: +86-17635110963

Abstract

The discrete element method (DEM) is widely used to simulate concrete failure, but calibrating its mesoscopic dynamic parameters is computationally expensive due to the high-dimensional parameter space. This study proposes a physics-informed active learning framework to autonomously calibrate these parameters under impact loads. An FDM-DEM coupled split Hopkinson pressure bar model is established to simulate macroscopic dynamic compressive responses. Subsequently, a Plackett–Burman experimental design reduces the parameter optimization space from 16 to 8 core dimensions. A multi-layer perceptron surrogate model is then constructed. By comparing two heuristic active sampling strategies, results indicate that a parameter priority-guided strategy incorporating physical priors significantly outperforms a mid-value exploration strategy. The proposed approach achieves coefficients of determination exceeding 0.9 for predicting multiple macroscopic dynamic indicators on an independent testing set. Building upon this forward mapping, a robust inverse parameter prediction mechanism is established, achieving a closed-loop reconstruction of 0.8662. This framework provides a reliable, data-efficient, and automated pathway for calibrating complex multiphase particulate systems.

Keywords: DEM; multiphase concrete; parameter calibration; active learning

1. Introduction

Concrete is widely used in various applications, including nuclear power plants, bridges, and high-rise buildings. The damage behavior of it under strong dynamic loads, including explosions, impacts, and high-frequency earthquakes, is critical for enhancing structural resilience and mitigating risks.

The discrete element method (DEM) has extensive applications in examining the dynamic behavior of concrete owing to its ability to simulate its failure processes [1–3]. However, concrete is a heterogeneous composite material with rate-dependent behavior, resulting in increased dynamic strength at higher loading rates [4]. Only by establishing an accurate geometric model that captures the nature of concrete as a heterogeneous composite material and carefully selecting DEM contact models and parameters can accurate and meaningful simulation results be obtained. Therefore, the efficient selection of appropriate DEM models and parameters to accurately reflect the bulk dynamic behavior of concrete remains an ongoing challenge.

Check for updates

Academic Editor: Giuseppe Quaranta

Received: 11 April 2026
Revised: 22 April 2026
Accepted: 23 April 2026
Published: 27 April 2026

Copyright: © 2026 by the authors. Licensee MDPI, Basel, Switzerland. This article is an open access article distributed under the terms and conditions of the Creative Commons Attribution (CC BY) license.

In the investigation of concrete dynamic behavior using DEM, the bonded particle model (BPM) is the most widely used [5,6]. However, the BPM has various parameters, and most scholars calibrate them through the traditional trial-and-error method [1–3]. The trial-and-error method is an iterative process in which DEM micro-parameters are manually refined until the simulated macroscopic responses converge with the experimental results [7,8]. Although easily understood, the trial-and-error approach is cumbersome and lacks scientific rigor. Its computational and labor costs, driven by the high-dimensional parameter space and expensive simulations, severely compromise calibration accuracy. This limitation is particularly acute for concrete's dynamic behavior. Some quasi-static experiments, such as biaxial, triaxial, and Brazilian splitting tests, are used to calibrate the dynamic DEM parameters [9–12], but these methods cannot accurately determine particle-scale dynamic parameters for concrete under dynamic loading. Although some scholars have employed inverse methods to establish correlations between dynamic macro-properties and micro-parameters [13], the process is often cumbersome, frequently requiring multiple software packages, thereby posing a significant barrier for many DEM users.

Given the challenges associated with both trial-and-error and inverse methods, the Design of Experiments (DoE), such as Taguchi methods, Plackett–Burman (PB), and Central Composite Design (CCD) [14,15], has emerged in recent years as a structured framework for calibrating DEM parameters. By establishing a quantitative micro-macro relationship, this method transforms parameter calibration into a mathematical optimization problem, thereby dramatically reducing the required time. However, the applicability of DoE is constrained by several inherent limitations. The correlations derived through DoE are model-specific and only valid within pre-defined parameter ranges, with deviations potentially leading to significant inaccuracies [16]. Moreover, the method shows limited proficiency in handling non-linear problems [17], and its performance further declines in systems with strong variable interactions or high structural complexity. The challenge of high-dimensional parameter spaces to DoE effectiveness becomes especially pronounced in the calibration of concrete numerical models, which involve distinct material phases [16,18].

Building on this foundation, deep learning and intelligent algorithms have advanced rapidly, offering new paradigms for mechanical parameter identification and structural analysis. In the context of DEM calibration, machine learning techniques, including Artificial Neural Networks (ANN) [19], Radial Basis Function Neural Networks (RBFNN) [20,21], and Random Forests (RF) [22], have been increasingly employed to bypass explicit theoretical formulations by learning directly from numerical data. Beyond traditional predictive modeling, the deep integration of intelligent algorithms with structural mechanics has shown tremendous potential. For instance, Wang et al. [23] recently proposed a structural performance warning framework based on computer-intelligent monitoring and fractional-order multi-rate Kalman fusion, representing a typical paradigm of utilizing data-driven methods for structural performance assessment. Furthermore, to address the computational burden of generating massive datasets, recent studies have emphasized the importance of data quality and complexity optimization. Research has demonstrated that reducing dataset Kolmogorov complexity, which essentially means minimizing the shortest algorithmic program required to produce the output, can lead to rapid accuracy gains in predictive models, even with constrained dataset sizes [24,25]. Despite these advancements, purely data-driven methods for DEM calibration generally suffer from a strong dependence on massive, high-quality training data and often lack underlying physical interpretability. These limitations collectively highlight a critical research gap in developing reliable, data-efficient, and physically constrained calibration frameworks for complex multiphase particulate systems, particularly for the high-dimensional DEM model of concrete.

To address this challenge, this study employs active learning (AL) [26,27], a data-efficient technique widely applied across scientific domains, to carefully calibrate the particle-scale dynamic parameters of the different phases in the concrete numerical model. Active learning iteratively selects the most informative samples to query for labeling [28,29]. Unlike traditional passive learning methods that operate on fixed, pre-collected datasets, this framework enables the model to autonomously detect regions of high uncertainty within the data and strategically query additional labels to resolve these ambiguities. By focusing on the most informative instances, the technique diminishes the reliance on extensive datasets that often incorporate substantial redundant or non-informative samples.

This study proposes a highly efficient, physics-informed active learning framework to autonomously calibrate the high-dimensional mesoscopic dynamic parameters of a multiphase concrete model. Specifically, an FDM-DEM coupled numerical approach is initially established to accurately simulate the macroscopic dynamic compressive responses of concrete under various impact strain rates. To overcome the computational bottleneck caused by the high-dimensional parameter space, a Plackett–Burman experimental design is utilized to screen and isolate the most influential mesoscopic contact parameters. Subsequently, an enhanced multi-layer perceptron is constructed as a surrogate model to approximate the complex non-linear mappings. By systematically integrating and comparing two distinct heuristic exploration strategies—a parameter priority-guided strategy and a mid-value specific exploration strategy—the active learning framework intelligently queries the most informative parameter combinations for high-fidelity physical simulation. The performance of these strategies is rigorously evaluated by tracking the dual convergence trajectories of training and validation errors, as well as the ultimate predictive fidelity on testing datasets. Ultimately, based on the optimal forward mapping foundation, a robust inverse prediction mechanism is established, enabling the direct and precise derivation of mesoscopic parameters from targeted macroscopic dynamic responses.

2. Methodologies

In the DEM, establishing a robust numerical model for concrete is essential for the careful calibration of particle-scale parameters. Since concrete is typically regarded as a three-phase composite material at the meso-scale, consisting of cement mortar, coarse aggregate, and the interfacial transition zone (ITZ) between them, the accuracy of the numerical model highly depends on two critical aspects: the realistic geometric representation of the aggregate and the appropriate selection of contact models for the different phases [2,30]. Only by constructing an accurate geometric model that reflects the meso-structure of concrete, combined with carefully chosen contact models and properly calibrated parameters, can meaningful and reliable simulation results be achieved. Therefore, this section primarily addresses the selection of the DEM contact models and the development of the concrete and SHPB numerical models.

2.1. The Parallel Bond Model of DEM

This study employs the parallel bond model (PBM) [11] to simulate the mechanical behavior of a cement-like material that binds particles together. This choice is justified due to the model's well-established calibration procedures, relatively low computational cost, and its broad validation in reproducing the macroscopic mechanical response of rock materials [11]. The PBM represents this material as a finite-sized elastic bond that transmits both force and moment between particles. Its formulation combines a linear elastic, tensionless interface with a frictional interface. For more details, the mechanical equations governing the forces and displacements of particles and cements can be referred to [11].

The mechanical behavior of the PBM assembly, illustrated in Figure 1, is governed by two distinct parameter sets for the particles and the cement-like material, respectively. The particle parameters include the Young's modulus E_c, the shear-to-normal stiffness ratio k_s/k_n, and the friction coefficient μ. The cement parameters comprise the Young's modulus $\overline{E}_c$, the shear-to-normal stiffness ratio $\overline{k}_s/\overline{k}_n$, the radius multiplier $\overline{\lambda}$, the tensile strength $\overline{\sigma}_c$, and the shear strength $\overline{\tau}_c$.

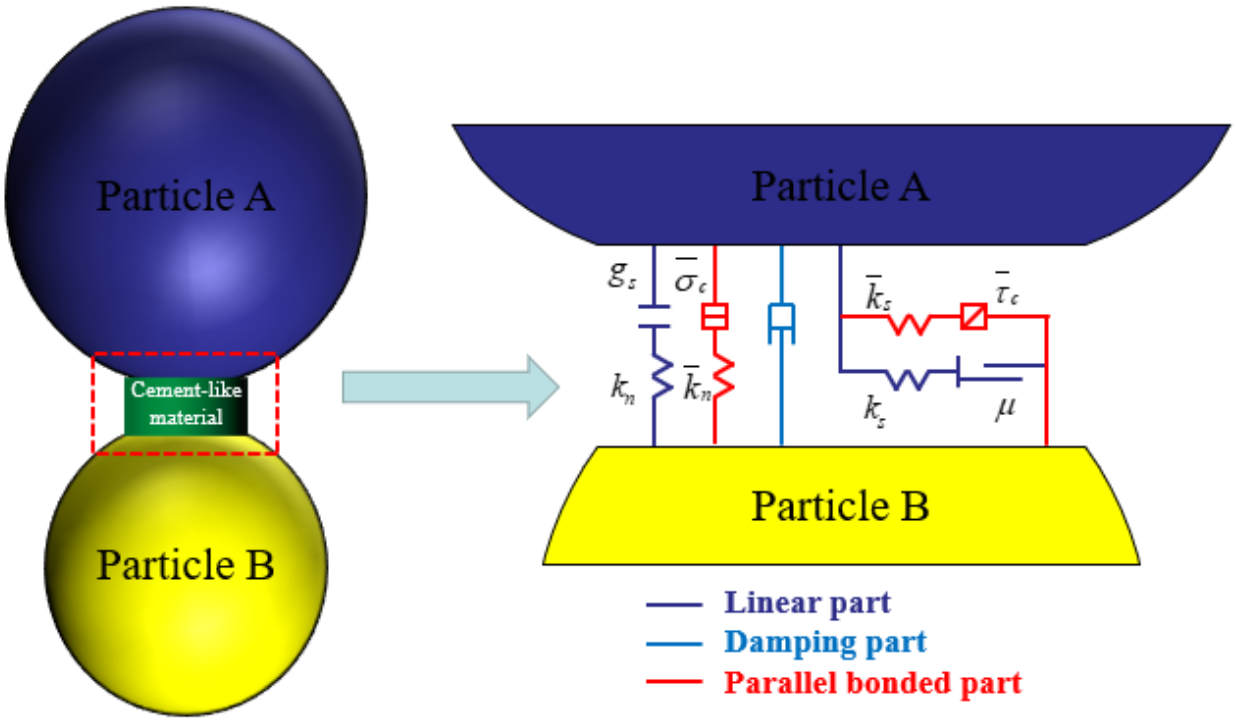


Figure 1. Microstructure of the parallel bonded model.

2.2. Construction of a Three-Phase Mesoscale Model for Concrete

The DEM models concrete as a three-phase meso-structure comprising cement mortar, coarse aggregate, and the ITZ. Accurately simulating the morphology and distribution of aggregates is crucial for mesoscale concrete models, as it essentially determines ITZ properties, such as location and shape, constituting a pivotal challenge in numerical modeling. In this work, to ensure consistency with real-world engineering conditions, the 3D aggregates were modeled as a convex polyhedron with a volume fraction of 40%. The large, medium, and small aggregates have particle sizes of 10.0~15.0 mm, 7.5~10.0 mm, and 5.0~7.5 mm, respectively. Their gradation followed a ratio of 4:3:3, conforming to the Fuller gradation curve [31], as follows:

$$P = \sqrt{\frac{D}{D_{\max}}} \tag{1}$$

where D is the preset aggregate diameter, P is the mass percentage of aggregates passing a sieve diameter D, and $D_{\max}$ is the maximum aggregate size.

A parametric modeling approach, based on the Monte Carlo method, is implemented via an in-house code to generate random aggregates within a specified domain. The procedure consisted of the following steps: (1) defining the placement region; (2) determining the centroid coordinates of the aggregates and calculating their quantity; (3) placing aggregates and checking for overlaps, followed by the removal of any that violated the non-overlap criterion; and (4) repeating step (3) until the target volume fraction is achieved. The model is configured as a cylinder with dimensions of 120 mm in base diameter and 100 mm in height, resulting in the aggregate distribution shown in Figure 2.

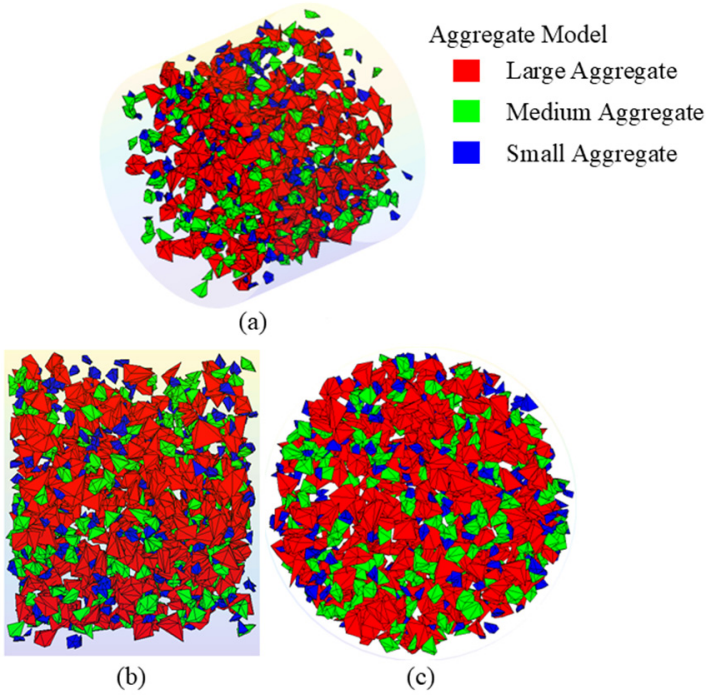


Figure 2. Distribution of random aggregates. (**a**) Axonometric View (**b**) Front View (**c**) Side View.

Within the cylindrical boundary of the geometric model, particles with radii uniformly distributed between 0.9 mm and 1.62 mm are randomly generated. They are classified as either aggregate or cement mortar particles based on whether their centers lie inside or outside the predefined aggregate volumes. The inter-particle contact is modeled using a linear parallel bond model. Different meso-parameters are assigned to three distinct contact types: aggregate–aggregate (aggregate bond), mortar–mortar (mortar bond), and aggregate–mortar (ITZ bond) contacts. The established mesoscopic particle model is shown in Figure 3.

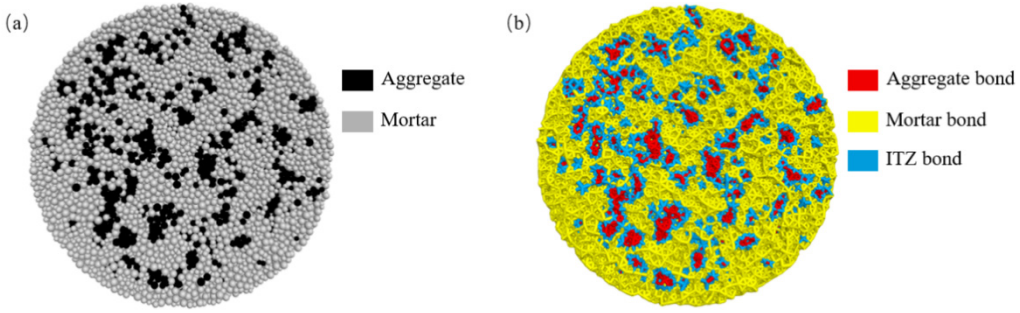


Figure 3. Cross-sectional view of the mesoscopic concrete model. (**a**) Particle diagram (**b**) bond diagram.

2.3. Establishment of the SHPB Device Through the FDM-DEM Coupled Method

As shown in Figure 4, a schematic of the large-diameter SHPB apparatus is used for dynamic compression tests. The system primarily consists of a loading subsystem (gas chamber, launcher, and striker), a stress transmission subsystem (incident and transmitted bars, along with a shock absorber), and a data acquisition subsystem (comprising strain gauges, an ultra-dynamic strain gauge, an oscilloscope, and a computer). Accordingly, a corresponding SHPB numerical model, constructed by coupling the Finite Difference Method and Discrete Element Method (FDM-DEM), is illustrated in Figure 5.

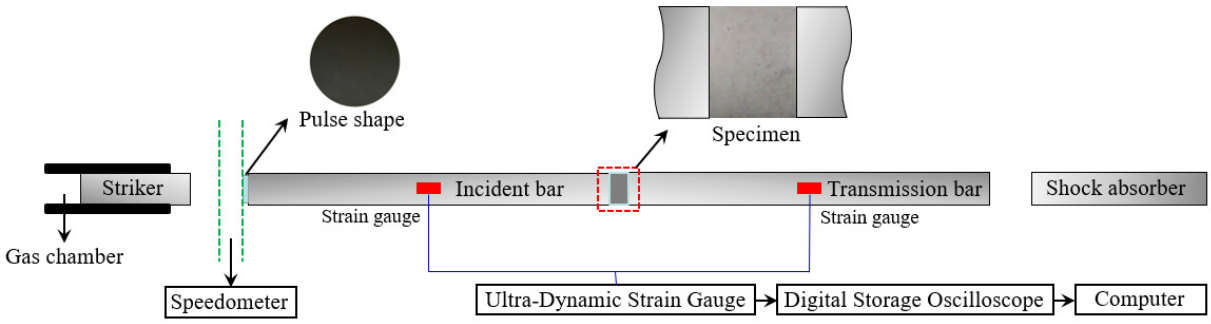


Figure 4. Schematics of the SHPB system.

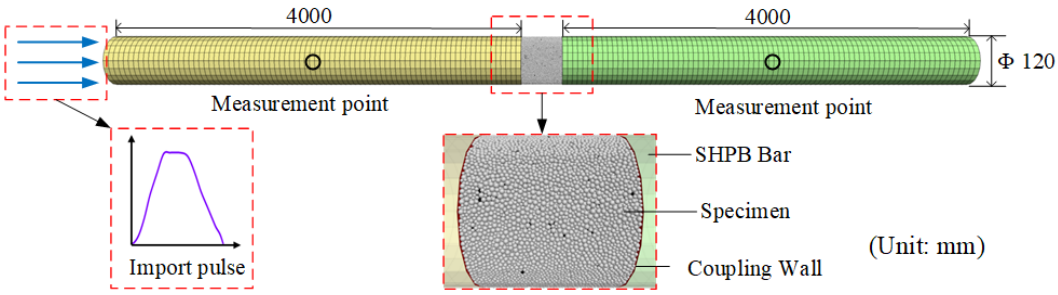


Figure 5. The three-dimensional numerical model of the SHPB device and concrete specimen.

The numerical model is constructed to adhere strictly to the geometric dimensions of the physical SHPB bars and specimen. In this coupled setup, the incident and transmitted bars are modeled as FDM zone elements, while the concrete specimen is represented via DEM. A wall–zone coupling interface at their contacts facilitates the transfer of forces and displacements.

To simplify the model, the striker's launch is not explicitly simulated. Instead, a physically measured incident stress wave from the SHPB test is directly applied as the force boundary condition at the free end of the incident bar. This approach ensures that wave propagation, including reflection and transmission at interfaces, is driven by a realistic input, thereby enhancing the reliability. A portion of the incident pulse reflects at the bar-specimen interface, while the remainder propagates into the specimen. Pulses are monitored at the midpoint of each bar.

3. A Data-Driven Model for Predicting Dynamic Bonded Parameters of a Three-Phase Mesoscale Model

3.1. Identification of Significant Input Parameters

Section 2.2 presents a three-phase mesoscale concrete model. As calibration involves multiple parameters and dynamic compressive strength serves as the response variable, a screening technique is essential to identify the parameters that most significantly influence this mechanical property, which is critical for accurately calibrating the model's dynamic parameters. Based on standard bonded particle model practices for multiphase composite materials, an initial comprehensive set of sixteen candidate parameters is defined, encompassing the stiffness and strength components of the aggregate, mortar, and ITZ contacts. For this purpose, the Plackett–Burman fractional factorial design is selected for this task. Requiring only a limited number of experimental runs, this screening approach efficiently isolates the key parameters from the candidate pool by exclusively estimating their main effects [32]. Although this design with 20 runs cannot capture complex parameter interactions, it is utilized here strictly as a preliminary screening tool. Given the high computational cost of 3D dynamic simulations, this represents a necessary compromise to

isolate the primary drivers. The subsequent multi-layer perceptron is specifically tasked with capturing the non-linear interactions among the remaining core parameters.

Within this modeling framework, the candidate parameters pertain to three interfacial contact types: aggregate-bond, mortar-bond, and ITZ-bond. The specific parameters and their feasible ranges, derived from established literature [1,3,9,33,34], are compiled in Table 1.

Table 1. Discrete element parameter level.

Parameter	Unit	Code	Low Level (−1)	High Level (+1)
Aggregate-bond				
E_C	GPa	A	10	50
k_s/k_n	-	B	1.3	1.9
$\overline{E}_C$	GPa	C	20	60
$\overline{k}_s/\overline{k}_n$	-	D	1.3	1.9
σ_c	MPa	E	30	60
τ_c	MPa	F	30	60
Mortar-bond				
E_C	GPa	G	5	25
k_s/k_n	-	H	1.3	1.9
$\overline{E}_C$	GPa	I	10	30
$\overline{k}_s/\overline{k}_n$	-	J	1.3	1.9
σ_c	MPa	K	15	30
τ_c	MPa	L	15	30
ITZ-bond				
$\overline{E}_C$	GPa	M	3	15
$\overline{k}_s/\overline{k}_n$	-	N	1.3	1.9
σ_c	MPa	O	10	20
τ_c	MPa	P	10	20

To evaluate the main effects of these 16 parameters, a Plackett–Burman (PB) experimental design matrix is constructed. Given that the PB design requires the number of runs to be a multiple of 4, a total of 20 independent FDM-DEM coupled dynamic impact simulations are systematically executed. In each simulation run, the candidate parameters are configured to either their predetermined high (+1) or low (−1) levels. The macroscopic peak compressive strength of the specimen under a specific dynamic strain rate of 85 s^{-1} is extracted and recorded as the key response variable for the sensitivity analysis. It is important to clarify that while the final active learning training and model verification incorporate dynamic response data from three distinct strain rates (40 s^{-1}, 85 s^{-1}, and 130 s^{-1}), the preliminary Plackett–Burman screening is intentionally conducted solely at the intermediate rate of 85 s^{-1}. Because these three conditions all belong to the medium to high velocity impact regime, selecting the intermediate strain rate effectively represents the overall dynamic properties of the parameters. This strategic choice actively prevents the dimensional explosion that would occur if screening was performed across multiple rates simultaneously, thereby ensuring a rapid, accurate, and highly efficient isolation of the critical parameters for the subsequent machine learning phase. The detailed experimental design matrix, along with the corresponding simulation results and calculated contribution rates, is presented in Table 2.

Table 2. Simulation run details in the Plackett–Burman test.

Run No.	A	B	C	D	E	F	G	H	I	J	K	L	M	N	O	P	Dynamic Strength (MPa)
1	1	1	1	−1	1	1	−1	1	−1	1	−1	−1	−1	−1	1	1	98.16
2	1	1	−1	1	1	−1	1	−1	1	−1	−1	−1	−1	1	1	1	86.43
3	1	−1	1	1	−1	1	−1	1	−1	−1	−1	−1	1	1	1	1	84.82
4	−1	1	1	−1	1	−1	1	−1	−1	−1	−1	1	1	1	1	1	136.45
5	1	1	−1	1	−1	1	−1	−1	−1	−1	1	1	1	1	1	−1	132.68
6	1	−1	1	−1	1	−1	−1	−1	−1	1	1	1	1	1	−1	1	134.79
7	−1	1	−1	1	−1	−1	−1	−1	1	1	1	1	1	−1	1	1	136.48
8	1	−1	−1	−1	−1	−1	−1	1	1	1	1	1	−1	1	1	1	138.68
9	−1	−1	−1	−1	−1	−1	1	1	1	1	1	−1	1	1	1	1	97.31
10	−1	−1	−1	−1	−1	1	1	1	1	1	−1	1	1	1	1	−1	103.82
11	−1	−1	−1	−1	1	1	1	1	1	−1	1	1	1	1	−1	1	125.46
12	−1	−1	−1	1	1	1	1	1	−1	1	1	1	1	−1	1	−1	171.18
13	−1	−1	1	1	1	1	1	−1	1	1	1	1	−1	1	−1	1	127.61
14	−1	1	1	1	1	1	−1	1	1	1	1	−1	1	−1	1	−1	85.52
15	1	1	1	1	1	−1	1	1	1	1	−1	1	−1	1	−1	1	114.68
16	1	1	1	1	−1	1	1	1	1	−1	1	−1	1	−1	1	−1	82.94
17	1	1	1	−1	1	1	1	1	−1	1	−1	1	−1	1	−1	1	142.65
18	1	1	−1	1	1	1	1	−1	1	−1	1	−1	1	−1	1	−1	81.75
19	1	−1	1	1	1	1	−1	1	−1	1	−1	1	−1	1	−1	1	127.41
20	−1	−1	−1	−1	−1	−1	−1	−1	−1	−1	−1	−1	−1	−1	−1	−1	81.68
Contribution (%)	2.32	1.38	0.32	2.56	8.45	6.47	3.69	6.71	1.01	9.75	5.00	13.09	6.74	11.95	8.62	11.91	

Following the completion of the 20 simulation runs, the main effect of each micro-parameter and its relative contribution to the macroscopic response are quantitatively assessed. To visualize the relative significance of these 16 microscopic parameters and facilitate the screening process, a Pareto chart of factor sensitivity is constructed, as illustrated in Figure 6.

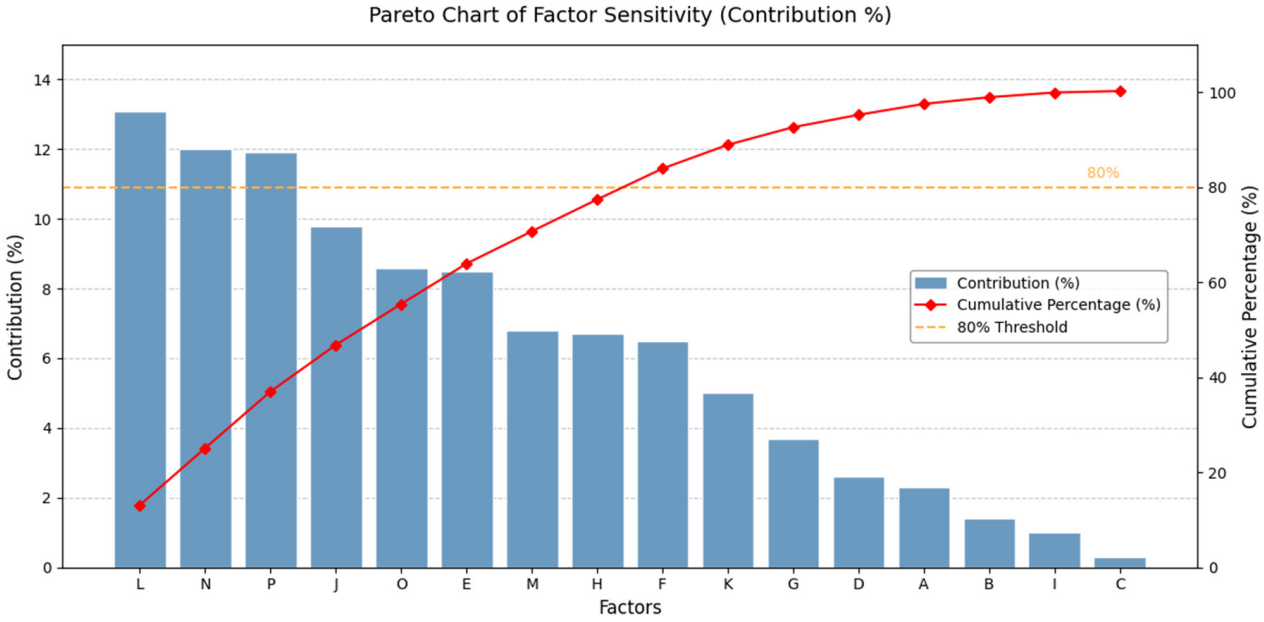


Figure 6. Pareto chart of factor sensitivity illustrating the main effect contributions and cumulative percentage.

The Pareto chart graphically ranks the parameters in descending order of their individual main effect contributions, accompanied by a cumulative percentage curve. As shown in the figure, the parameter space exhibits a strong Pareto principle, where a subset of variables dictates the majority of the macroscopic dynamic response. The relative contribution intuitively reflects the average variation in the macroscopic dynamic compressive strength when a specific parameter shifts from its low to high level. To effectively eliminate the computational interference of low-sensitivity dimensions and isolate the variables

dominating the dynamic response, a preliminary screening threshold of a 5% main effect contribution is established.

Based on this visual and statistical analysis, the top ten parameters (from L to K in Figure 6) all meet or exceed this 5% threshold, cumulatively accounting for approximately 88% of the total systemic variance. However, because the cement mortar matrix constitutes the largest volume fraction within the multiphase concrete composite, its corresponding stiffness ratio (Parameter H, contribution 6.71%) and bond stiffness ratio (Parameter J, contribution 9.75%) overwhelmingly govern the macroscopic static elastic deformation characteristics, such as the static Young's modulus and Poisson's ratio. Since the primary objective of this study focuses specifically on calibrating the dynamic compressive strength under impact loading, these two elastic parameters are excluded from the dynamic active learning calibration loop. To effectively reduce the dimensionality of the optimization space, they are instead pre-calibrated via standard quasi-static compression simulations and subsequently kept constant.

Consequently, after excluding parameters H and J, eight core micro-parameters that definitively control the dynamic peak strength at 85 s^{-1} are identified. Ranked by their relative significance, the most influential factor is the mortar microscopic shear strength (Parameter L), which contributes 13.09% to the main effect. This is closely followed by the ITZ bond stiffness ratio (Parameter N) and the ITZ microscopic shear strength (Parameter P), demonstrating contributions of 11.95% and 11.91%, respectively. The subsequent critical parameters include the ITZ microscopic tensile strength (Parameter O) at 8.62%, the aggregate microscopic tensile strength (Parameter E) at 8.45%, the ITZ effective bond modulus (Parameter M) at 6.74%, and the aggregate microscopic shear strength (Parameter F) at 6.47%. Finally, the mortar microscopic tensile strength (Parameter K) serves as the last selected parameter with a 5.00% contribution.

The prominence of the four ITZ parameters (N, P, O, M) among the top contributors aligns perfectly with the physical failure mechanisms of concrete under dynamic loading. The ITZ inherently acts as the weakest link within the multiphase composite. Due to its relative structural weakness, the ITZ serves as the primary site for stress concentration. Consequently, macroscopic failure typically originates here, with microcracks preferentially initiating and propagating along these interfacial boundaries, making the ITZ properties disproportionately affect the overall macroscopic peak strength of the material. From a physical perspective, the ITZ bond stiffness ratio (Parameter N) and the effective bond modulus (Parameter M) fundamentally govern the local stress concentration and acoustic impedance mismatch during stress wave propagation. A severe impedance mismatch at the interface between aggregate and mortar accelerates localized damage. Concurrently, the ITZ microscopic shear strength (Parameter P) and tensile strength (Parameter O) directly dictate the threshold for microcrack initiation. Under high strain rate impact, the rapid accumulation and coalescence of these interfacial microcracks dominate the macroscopic dynamic failure envelope. Therefore, capturing the precise non-linear combinations of these four ITZ parameters is critical for accurately reproducing the dynamic compressive strength.

These eight critical micro-parameters are subsequently extracted to construct the reduced-dimensional parameter space for the data-driven active learning surrogate model and intelligent dynamic calibration. The remaining eight parameters (A, B, C, D, G, H, I, J), which predominantly govern the macroscopic static elastic deformation characteristics, were rigorously pre-calibrated utilizing a hybrid analytical and computational framework based on strain energy conservation principles [35–37]. Instead of relying on traditional iterative trial and error or empirical assignments, this advanced methodology establishes a direct theoretical correlation between the mesoscopic contact stiffnesses and the macro-

scopic elastic properties, specifically the static elastic modulus and Poisson's ratio. By equating the strain energy at the particle scale to that at the continuum scale, we analytically mapped and determined the exact values for these static parameters. Employing this rigorous mathematical framework ensured that the static mechanical behavior of the concrete specimen was accurately captured, achieving a matching error strictly below 3% against the experimental static targets. Since their cumulative contribution to dynamic strength variance is minimal, fixing these statically calibrated parameters during the subsequent dynamic simulations introduces negligible prediction error while drastically reducing optimization dimensionality. This strategy, which deeply integrates statistical sensitivity quantification with physical mechanism constraints, successfully reduces the high-dimensional parameter space from 16 to 8 dimensions, thereby establishing a solid foundation for efficient parameter inversion based on active learning.

3.2. Dataset Preparation and Preprocessing

To initialize the data-driven active learning framework, the mathematical structure of the machine learning task must be explicitly defined. The input feature vector, denoted as x, is strictly constructed using the eight core mesoscopic parameters successfully isolated through the Plackett–Burman sensitivity analysis. This high-dimensional feature vector is mathematically expressed as:

$$x = (x_1, x_2, x_3, x_4, x_5, x_6, x_7, x_8) = (E, F, K, L, M, N, O, P) \tag{2}$$

where the individual vector components correspond sequentially to the aggregate microscopic tensile strength, aggregate microscopic shear strength, mortar microscopic tensile strength, mortar microscopic shear strength, ITZ effective bond modulus, ITZ bond stiffness ratio, ITZ microscopic tensile strength, and ITZ microscopic shear strength. Conversely, to comprehensively capture the complex strain-rate dependency and failure behavior of the concrete composite, the output response vector, denoted as y, is explicitly defined to comprise six key macroscopic dynamic mechanical indicators extracted from the physical simulations. This specific multi-dimensional response vector is formulated as:

$$y = (y_1, y_2, y_3, y_4, y_5, y_6) = (\varepsilon_1, \sigma_1, \varepsilon_2, \sigma_2, \varepsilon_2, \sigma_2) \tag{3}$$

Consequently, the primary objective of the entire active calibration framework is to establish a robust nonlinear mapping relationship $f : R^8 \rightarrow R^6$ that accurately connects the mesoscopic input vector x to the macroscopic dynamic response vector y.

With the fundamental input–output structure defined, a comprehensive and representative database of matched data pairs is fundamentally required. Instead of relying on conventional random sampling, Latin Hypercube Sampling (LHS) is employed to carefully construct the initial parameter pool. LHS serves as an advanced stratified sampling technique that ensures a near-random yet highly uniform distribution of parameter combinations across the multi-dimensional design space. By dividing the feasible range of each of the eight core mesoscopic parameters into equal-probability intervals, LHS guarantees that the entire complex parameter space is efficiently explored without generating excessive computational redundancy. This generated pool effectively serves as the primary candidate database from which the active learning algorithm subsequently queries the most informative samples for physical FDM-DEM dynamic impact simulations.

Before actual network training, rigorous data preprocessing must be systematically executed on the generated database. The eight identified micro-parameters, such as the effective bond modulus and microscopic shear strength, possess vastly different physical units and numerical scales. If these raw values are directly utilized, the gradient descent

process during network optimization becomes disproportionately dominated by the parameters with larger absolute magnitudes, inevitably leading to severe training instability, sluggish convergence, and suboptimal predictive performance. To effectively mitigate this numerical discrepancy, a Min-Max normalization procedure is applied to linearly scale all input features into a standardized dimensionless interval ranging from 0 to 1. The normalization process for any arbitrary parameter x is mathematically expressed as:

$$x_{norm} = \frac{x - x_{\min}}{x_{\max} - x_{\min}} \tag{4}$$

where $x_{\min}$ and $x_{\max}$ denote the predetermined lower and upper boundaries of that parameter's specific feasible range, respectively, and x_{norm} represents the resulting scaled value. This essential normalization step mathematically guarantees that the subsequent surrogate model evaluates every parameter dimension equitably, significantly reducing the condition number of the input feature matrix and substantially improving the overall generalization stability of the data-driven framework.

3.3. Construction of the Data-Driven Prediction Model

To efficiently establish the complex non-linear mapping between the mesoscopic parameters and the macroscopic dynamic response, a surrogate model based on a multi-layer perceptron is developed. The constructed multi-layer perceptron is a fully connected feedforward artificial neural network highly capable of approximating intricate multi-dimensional data relationships without requiring explicit mathematical formulations. The network topology is explicitly designed to match the dimensionality of the dynamic calibration task. Specifically, the input layer consists of exactly eight neurons, which correspond directly to the eight core micro-parameters identified in the previous sensitivity analysis. Conversely, the output layer is precisely configured to yield six macroscopic predictions representing the dynamic mechanical indicators under specific impact loading conditions. Between the precisely defined input and output layers, three hidden layers containing 16, 12, and 8 neurons, respectively, are deployed. These layers progressively extract and synthesize deep, interacting features from the highly coupled input variables, using the hyperbolic tangent activation function to robustly capture the severe nonlinear dynamics inherent in multiphase concrete impact interactions. The schematic diagram of the constructed MLP network topology is illustrated in Figure 7.

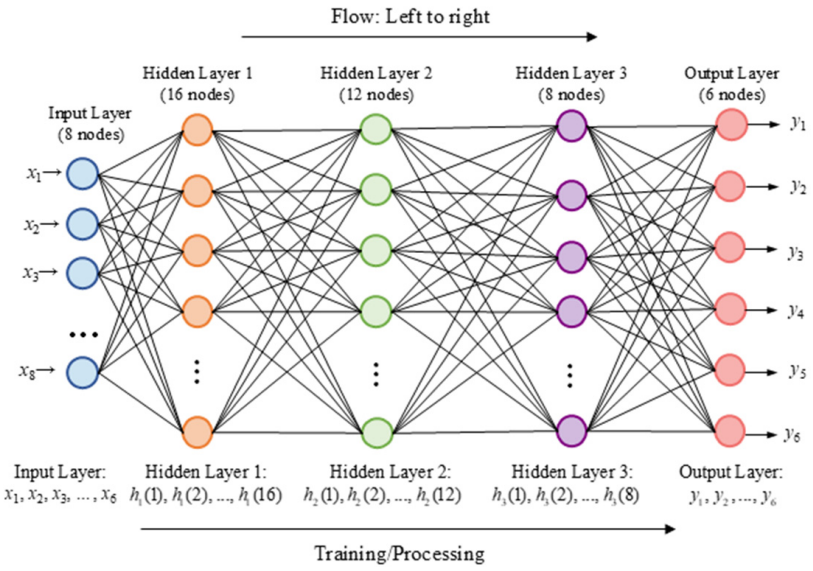


Figure 7. Schematic diagram of the multi-layer perceptron surrogate model.

To fully explore the predictive performance of the proposed surrogate model during the training process and to ensure the accuracy and reliability of the final calibration results, the mean squared error and the mean absolute error are adopted as two distinct metrics for comprehensive assessment. During the model training process, the mean squared error is selected as the primary loss function. Because this metric exerts a strong penalizing effect on samples with large errors, it effectively guides the model to converge rapidly in the early stages and promptly correct substantial prediction deviations. The specific formula for the mean squared error is mathematically defined as:

$$MSE = \frac{1}{n}\sum_{i=1}^{n}(\hat{y}_i - y_i)^2 \tag{5}$$

where n denotes the total number of samples, while y_i and $\hat{y}_i$ represent the true actual value and the predicted value generated by the model, respectively. To drive the internal training process based on this loss function, the Adam optimization algorithm is utilized to iteratively update the network weights and biases. To further enhance training stability and prevent the potential issue of exploding gradients commonly encountered in deep networks, a gradient clipping mechanism is effectively incorporated into the backpropagation process, thereby ensuring robust and mathematically stable calibration.

Conversely, to ensure that the evaluation of the model's final performance is not overly dominated by individual outlier samples, and to more intuitively reflect the average degree of deviation between the predicted values and the true values, the mean absolute error is selected as the final evaluation metric. The specific formula for the mean absolute error is defined as:

$$MAE = \frac{1}{n}\sum_{i=1}^{n}|\hat{y}_i - y_i| \tag{6}$$

While the constructed surrogate model provides robust predictions, traditional passive machine learning methods still rely heavily on massive static datasets, which remain computationally prohibitive when each underlying data point necessitates an expensive dynamic impact simulation. To overcome this fundamental bottleneck, an adaptive hybrid active sampling framework is seamlessly integrated. This framework iteratively evaluates vast pools of unlabeled parameter combinations and strategically queries only the most informative samples for actual physical simulation. To optimize this precise selection process, a comprehensive acquisition function is defined to evaluate any unlabeled candidate sample x. This mathematical framework combines multiple criteria to calculate an overarching utility score, which is mathematically formulated as:

$$S(x) = \alpha \cdot \hat{U}(x) + \beta \cdot \hat{E}(x) + \gamma \cdot \hat{D}(x) \tag{7}$$

In this equation, $\hat{U}(x)$, $\hat{E}(x)$, and $\hat{D}(x)$ represent the normalized prediction uncertainty score, feature exploration score, and spatial diversity score, respectively. The coefficients α, β, and γ denote the respective weighting factors. To maintain a stable evaluation baseline, the uncertainty weight α and the spatial diversity weight γ are fixed at 0.4 and 0.3, respectively. The heuristic exploration weight β is adaptively adjusted based on the current cognitive state of the model, specifically utilizing the proportion of mid-value samples in the labeled dataset as the core regulatory metric. The adaptive mechanism dynamically restricts β between a minimum of 0.1 and a maximum of 0.4. If the mid-value proportion falls below 0.3, indicating a severe lack of central exploration, β is proportionally elevated to prioritize spatial domain expansion. Once this proportion exceeds 0.6, signifying adequate central coverage, β immediately drops to its minimum value of 0.1 to favor local exploitation. Between these two thresholds, β is smoothly adjusted using linear interpolation.

This data-driven piecewise mechanism ensures a seamless and mathematically rigorous transition between global exploration and localized boundary exploitation throughout the iterative calibration process. This comprehensive acquisition function integrates the prediction uncertainty to identify unknown boundary regions, the spatial diversity to prevent redundant localized sampling, and the specially designed heuristic exploration term to actively guide the physical learning trajectory based on structural and geometric priors.

Within this mathematical evaluation context, two distinct heuristic search strategies are developed to explicitly define the heuristic exploration mechanism $\hat{E}(x)$. The first approach is a parameter priority-guided strategy, which fundamentally relies on the intrinsic physical priors of the concrete composite. Instead of treating all parameter dimensions uniformly, this strategy seamlessly integrates a predefined priority weight vector into the active sampling distribution. Based on the physical mechanism constraints, the fundamental mortar matrix parameters are designated the highest priority weight of 1.0, followed by the aggregate strength parameters assigned a weight of 0.8. The interfacial transition zone effective modulus is given a moderate weight of 0.6, while the highly localized and variable microscopic strength parameters of this zone receive the lowest weight of 0.4. By embedding these predetermined weights into the algorithm, the comprehensive priority-guided evaluation score $E_P(x)$ for a given candidate sample is mathematically calculated by accumulating the weighted dimensions, expressed as:

$$E_P(x) = \sum_{i=1}^{8} W_i \cdot I(x_i) \cdot (1 + R_{mid}(x_i)) \tag{8}$$

where x_i represents the i-th dimensional feature of the candidate sample, and $I(x_i)$ serves as a matching indicator function. In the algorithmic execution, the strategy analyzes the coverage of feature values in the labeled dataset in real-time, identifying unrepresented or extremely low-frequency parameter intervals as high-value exploration targets. When x_i successfully hits a high-value target, $I(x_i)$ equals 1; otherwise, it is 0. The coefficient W_i denotes the assigned priority weight for the i-th dimension, corresponding to the previously established four-tier hierarchy. Furthermore, $R_{mid}(x_i)$ acts as an incorporated superimposed score reward mechanism. If the hit exploration target precisely falls within the middle region of the parameter's value range, an extra numerical reward is granted; otherwise, it is set to 0. This mechanism effectively forces the surrogate model to prioritize the exploration of core mesoscopic parameters governing the macroscopic failure modes within a limited number of physical simulations.

The second approach is a mid-value specific exploration strategy. This alternative is purposefully designed to counteract the severe boundary-heavy sampling bias typically introduced by initial factorial screening designs, which predominantly test extreme upper and lower parameter limits. To effectively repair the resulting localized information vacuums and smooth the highly non-linear regression surface within the interior of the parameter space, this strategy mathematically encourages the active learning algorithm to target the central regions of the parameter tolerance zones. This strategy does not strictly require candidate samples to exactly hit the absolute mid-values. Instead, it introduces the concept of continuous tolerance relaxation, establishing an effective mid-value zone by setting a relative tolerance boundary. For the i-th feature value x_i of a candidate sample, its degree of closeness $C(x_i)$ to the respective feature mid-value μ_i is explicitly defined as:

$$C(x_i) = \max\left(0, 1 - \frac{|x_i - \mu_i|}{R_i \cdot \tau}\right) \tag{9}$$

where R_i represents the absolute range of the i-th feature's feasible values, and τ denotes the predefined relative tolerance ratio. This closeness metric is strictly bounded between 0 and 1, where a value of 1 indicates a perfect coincidence with the feature center, while a value of 0 signifies that the candidate sample falls entirely outside the specified tolerance calculation range. During the execution logic, the system initially conducts a weighted closeness assessment by combining the proximity of each feature with its corresponding priority weight to calculate the overall weighted mid-value closeness of the sample. To prevent the model from over-selecting samples tightly clustered around the absolute center, which would lead to information redundancy, the algorithm further incorporates an adaptive diversity penalty mechanism. When selecting sample batches, the system evaluates the mid-value quality in real-time; if the comprehensive closeness falls below an evaluation threshold, a stricter diversity distance boundary is enforced, compelling the candidate sample to maintain a sufficiently large Euclidean distance from already selected samples. This mechanism effectively repairs sample deficiencies in non-linear interpolation regions while simultaneously avoiding local overfitting risks through the diversity threshold. By strategically deploying these intelligent active sampling mechanisms throughout the calibration process, the surrogate model autonomously and efficiently navigates the high-dimensional parameter space, iteratively upgrading its overall predictive accuracy while successfully reducing the total number of expensive physical numerical simulations.

4. Implementation of an Active Learning Approach

Before the official execution of the automatic discrete element parameter calibration for the multiphase mesoscopic concrete under multi-strain-rate impacts, it is essential to macroscopically outline the core iterative logic of the constructed active learning framework. While traditional passive machine learning methods depend heavily on massive static training datasets, active learning fundamentally breaks this dependency paradox by establishing an intelligent closed-loop data acquisition flow consisting of generation, evaluation, annotation, and updating. This comprehensive framework maps several key physical nodes into the computational mechanics context. Specifically, the initial labeled dataset serves as the prior knowledge, corresponding to the 20 sets of FDM-DEM simulation results (cold-start data) generated via the Plackett–Burman experimental design. The massive unlabeled candidate pool consists of thousands of unknown parameter combinations generated by discretizing the core 8-dimensional parameter space. The predictive heart of the system is the machine learning surrogate model, represented by the enhanced multi-layer perceptron. Finally, the role of the human oracle or annotator in traditional active learning is perfectly substituted by the high-fidelity, though computationally expensive, three-dimensional FDM-DEM coupled dynamic impact simulation program. In terms of specific implementation details, a batch of exactly 4 highly informative parameter combinations is automatically selected and simulated during each active learning iteration. To ensure a rigorous and fair controlled experiment between the two distinct heuristic exploration strategies, the total number of active learning iterations is deliberately fixed at exactly 20 rounds for both groups. This uniformly constrained computational budget allows for a direct and objective comparison of their respective learning efficiencies under identical data acquisition limits. Consequently, exactly 80 newly queried physical simulations are added to the global database for each strategy.

Based on this closed-loop logic, a single active learning iteration proceeds through a systematic workflow, as visually summarized in Figure 8. First, the multi-layer perceptron surrogate model performs rapid forward inference on the massive unlabeled pool. By utilizing the adaptive hybrid sampling mechanism, the model quantitatively evaluates each candidate combination based on its prediction uncertainty, spatial diversity, and heuristic

exploration value. Subsequently, the algorithm automatically selects a small subset of candidate parameters that yield the highest comprehensive information gain—essentially identifying the data points that most urgently require high-fidelity "expert" annotation. These high-value parameters are then fed into the high-fidelity FDM-DEM model to execute actual time-history dynamic impact simulations, thereby acquiring their true macroscopic dynamic compressive strengths through physical simulation. Finally, these newly acquired mesoscopic-macroscopic data pairs are added to the labeled dataset, and the multi-layer perceptron is retrained and updated. This "query-as-you-learn" mechanism ensures that limited computational resources are strictly concentrated on the most fitting-intensive non-linear blind spots within the parameter space.

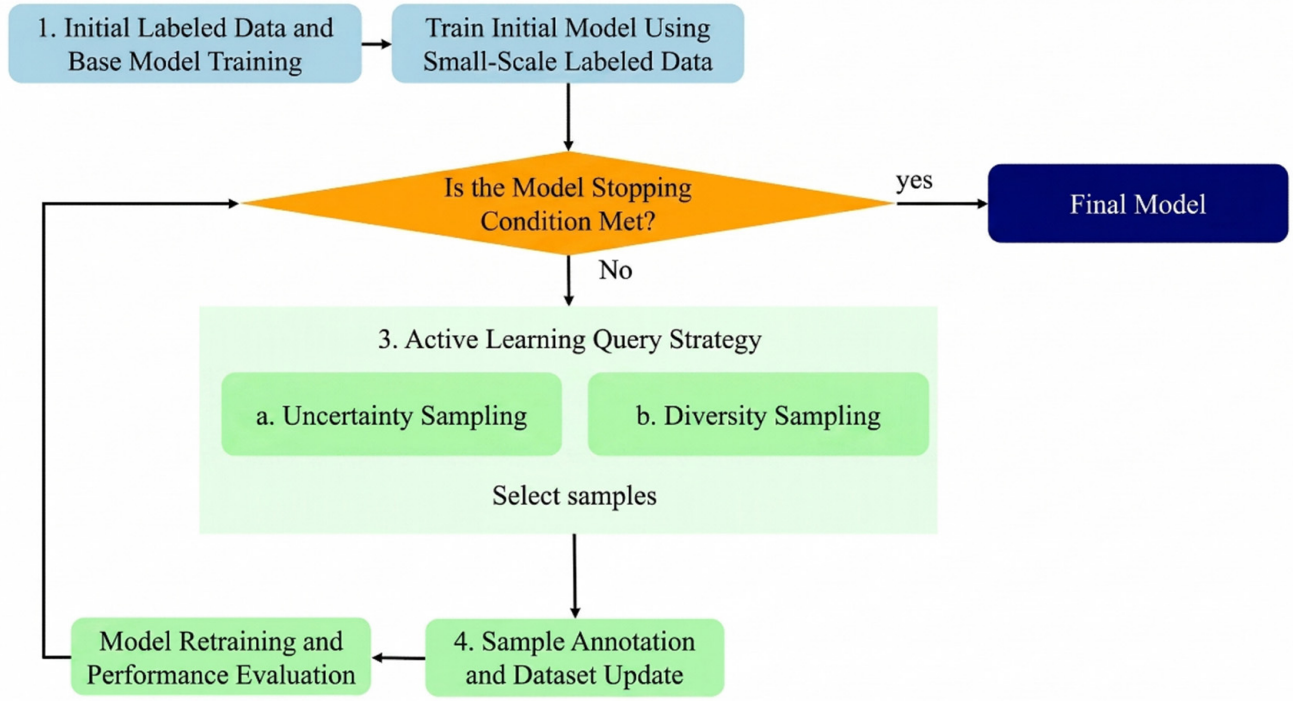


Figure 8. Flowchart of the proposed active learning framework for dynamic parameter calibration.

During the iterative evolution of the active learning process, the dual convergence trajectories of the underlying training MSE and the validation MAE are monitored, as illustrated in Figures 9 and 10. For the parameter priority-guided strategy, the training MSE exhibits a rapid decline from approximately 0.026 to 0.005 in the initial stage. This indicates that the quadratic amplification mechanism of the MSE effectively penalizes significant cognitive biases at the initial extreme boundaries, prompting rapid correction of the network weights. Simultaneously, the MAE of the independent validation set shows a highly synchronized and smooth downward trend, reaching approximately 0.09 by the fourth batch. This synchronous convergence between internal training error and external validation error confirms that the high-value physical samples selected by this strategy successfully mitigate the risk of overfitting in the deep network under sparse data conditions, leading to a steady improvement in the model's true generalization capability across unknown parameter landscapes. In the later stages of iteration, both error curves continue to decline gently, eventually stabilizing at 0.0048 and 0.1054, respectively, by the twentieth batch. This achievement is attributed to the feature importance prior, which accurately concentrates computational resources on high-sensitivity dimensions to solidly construct the decision boundaries for the core parameters.

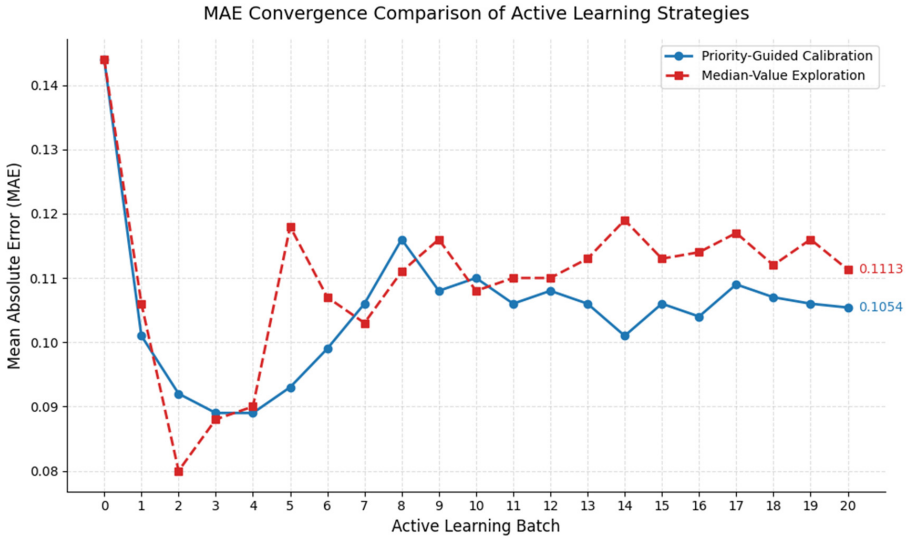


Figure 9. Convergence trajectories of validation MAE for the parameter.

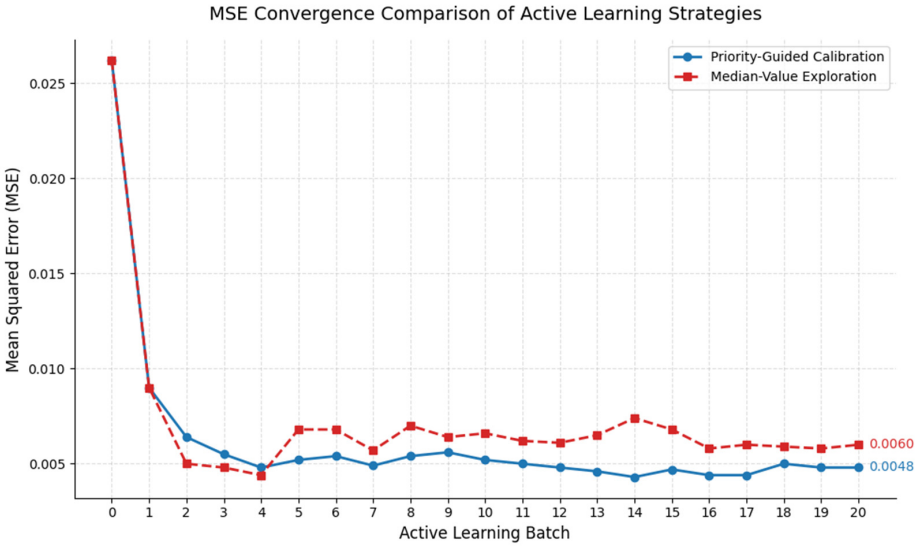


Figure 10. Convergence trajectories of training MSE for the parameters.

In contrast, the error evolution curve of the mid-value specific exploration strategy reveals that within the first four batches, the error reduction rate is slightly faster than that of the priority-guided strategy, with the validation MAE reaching a low of 0.08. This phenomenon proves that the mandatory supplementation of high-quality samples into the interior of the parameter space successfully fills the information vacuum left by the initial orthogonal design, yielding significant early information gains. However, during the middle stages of iteration, the validation MAE exhibits a notable rebound and remains in an oscillatory state throughout the subsequent iterations, finally converging to a value of 0.1113, which is higher than that of the priority-guided strategy. This mid-to-late-stage oscillation suggests that while the underlying adaptive diversity penalty mechanism forces the model to explore deep non-linear mapping regions to prevent premature convergence, these spatial exploration jumps partially disrupt the local smoothness of the core decision boundaries. Consequently, the inference bias on the validation set increases, sacrificing local fitting accuracy in the later stages.

To comprehensively and impartially evaluate the ultimate predictive fidelity of the surrogate models derived from different active sampling strategies, a rigorous post-processing assessment is conducted. Specifically, all newly queried data points actively sampled and

annotated by the high-fidelity FDM-DEM simulations throughout the iterative process are extracted. These dynamically acquired samples are then systematically merged with the initial 20 data points generated by the Plackett–Burman design to construct a complete, enriched global database for each respective strategy. Subsequently, to guarantee an unbiased performance evaluation, these enriched databases are rigorously re-partitioned into new independent training and testing sets. Fresh multi-layer perceptron models are then retrained from scratch using these newly split datasets. The actual testing performances of these retrained models across the six normalized macroscopic dynamic indicators (Y1 to Y6) are systematically evaluated and compared. The comprehensive scatter distributions mapping the true physical values against the network predictions for both strategies are illustrated in Figure 11.

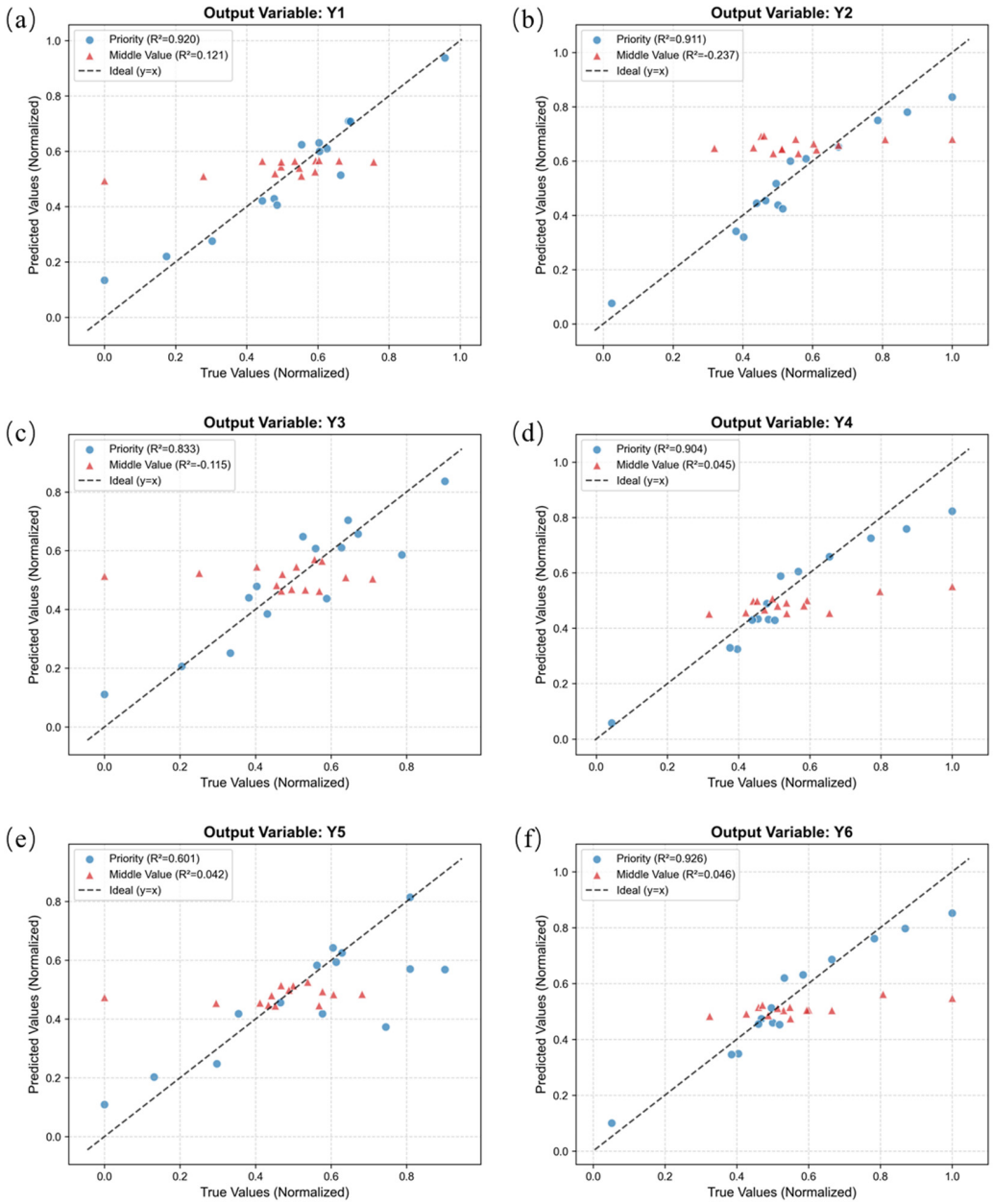


Figure 11. Scatter distributions of true vs. predicted values for the six macroscopic dynamic indicators (Y1 to Y6) based on retrained surrogate models. (**a**) output variable: Y1; (**b**) output variable: Y2; (**c**) output variable: Y3; (**d**) output variable: Y4; (**e**) output variable: Y5; (**f**) output variable: Y6.

To further explicitly quantify this performance disparity, a comprehensive side-by-side comparison of the coefficient of determination (R^2) scores across all six macroscopic variables is visually summarized in Figure 12. As visually confirmed by these scatter distributions and the accompanying bar chart, the parameter priority-guided strategy demonstrates exceptional predictive capabilities on the testing set. The predicted data points generated by this priority strategy (blue circles) tightly align with the ideal diagonal reference line across all dynamic indicators. Furthermore, its corresponding coefficient of determination (R^2) values are highly satisfactory, with the vast majority of targets exceeding 0.8. Specific macro-indicators, such as Y1 ($R^2 = 0.920$), Y2 ($R^2 = 0.911$), Y4 ($R^2 = 0.904$), and Y6 ($R^2 = 0.926$), remarkably surpass the 0.9 threshold. This robust correlation confirms that prioritizing the fundamental physical constraints successfully allows the network to capture the underlying severe non-linear dynamics and establish highly reliable global mapping boundaries. Conversely, the mid-value specific exploration strategy exhibits a catastrophic predictive failure on the testing set. Across all six macroscopic variables, the R^2 values of the mid-value strategy (red triangles) drastically plummet, predominantly hovering near zero or even dropping into negative territory, such as -0.237 for Y2 and -0.115 for Y3. The scatter distributions reveal a severe horizontal clustering phenomenon, where the model outputs nearly constant predictions regardless of the actual physical true values. This catastrophic predictive failure of the mid-value strategy warrants a deeper physical interpretation. The horizontal clustering is not merely a numerical regression artifact but a fundamental physical disconnect. The dynamic failure of concrete composites under high-strain-rate impacts, such as rapid microcrack coalescence and macroscopic fragmentation, is strictly governed by the extreme boundaries of the material strength envelope. By mathematically coercing the active sampling algorithm to exclusively explore the central regions of the parameter space, the mid-value strategy systematically starves the neural network of the critical extreme boundary information. Consequently, the surrogate model entirely fails to learn the correct physical performance gradients. This stark contrast strongly suggests that incorporating physical priority guidance is not merely an optimization enhancement but an absolute necessity for capturing the true dynamic failure envelope. Ultimately, this comparative analysis proves that the parameter priority-guided strategy is significantly superior, providing a robust, physics-informed data-driven pathway for the accurate dynamic calibration of the multiphase discrete element model.

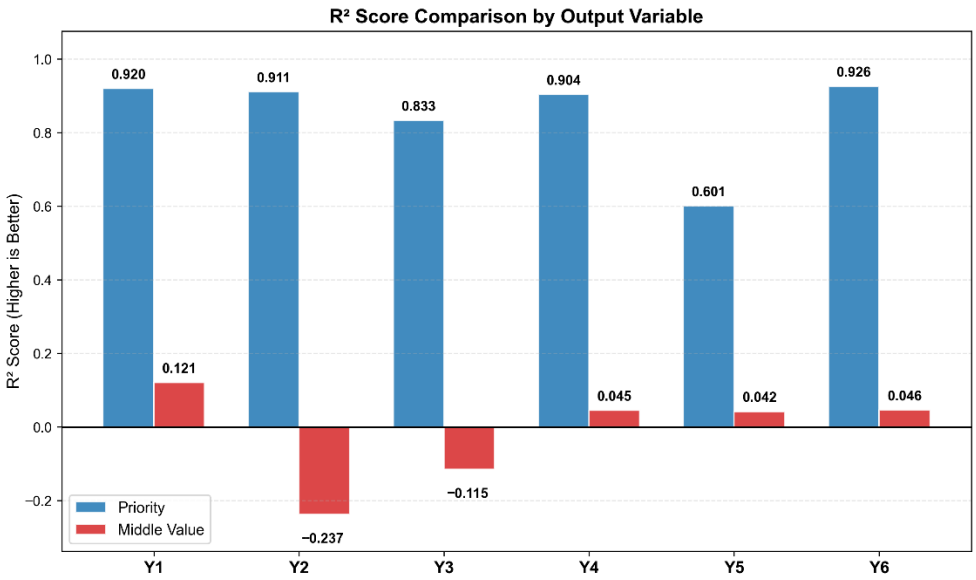


Figure 12. Comparison of R-squared scores across six macroscopic dynamic indicators for different sampling strategies.

Building upon this highly accurate forward mapping foundation established by the priority strategy, the core objective of this study further extends to constructing an inverse mapping mechanism from the macroscopic dynamic response back to the mesoscopic contact parameters. To achieve the precise prediction of physical properties from macroscopic mechanical targets, all high-quality forward simulation samples accumulated during the active learning optimization process are comprehensively extracted. To ensure an objective evaluation of model performance, the global dataset is strictly partitioned into independent training and testing sets. Following the training of an inverse multi-layer perceptron network based on this partitioned dataset, the training loss convergence trajectories mapping the macroscopic targets Y to the mesoscopic parameters X are continuously monitored, as depicted in Figure 13.

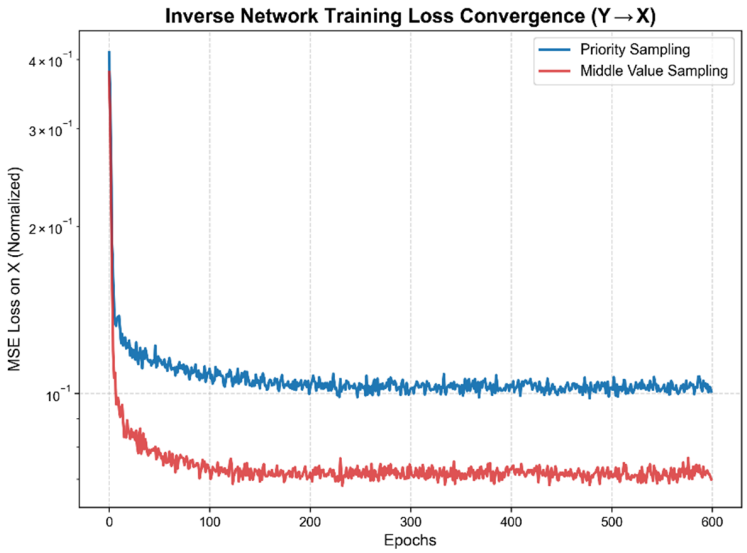


Figure 13. MSE training loss convergence trajectories for inverse mapping networks under different sampling strategies.

Analyzing the inverse loss curves reveals a critical phenomenon: while the mid-value specific exploration strategy appears to achieve a lower numerical mean squared error on the parameter space X, this minimization is highly deceptive. It merely reflects a severe localized clustering of its training samples artificially bounded near the parameter center, allowing the network to easily overfit a narrow variance rather than learning the global inverse physical rules. In stark contrast, the inverse training under the parameter priority-guided strategy exhibits a highly stable, mathematically robust convergence plateau, indicating a comprehensive, balanced mapping across the broader, high-dimensional parameter space.

Because the inverse parameter identification in granular materials is inherently an ill-posed computational problem characterized by non-unique solutions, directly evaluating the regression error solely within the parameter space X is fundamentally insufficient. To rigorously assess the engineering applicability of these trained inverse models, a closed-loop validation framework is implemented. In this validation flow, the predicted mesoscopic parameters $\hat{X}$ generated by the inverse network are subsequently fed back into the highly accurate forward surrogate model to calculate the reconstructed macroscopic dynamic responses $\hat{Y}$. The ultimate reliability of the inverse design is determined not by intermediate parameter errors, but by the physical consistency between these reconstructed responses $\hat{Y}$ and the original targeted macroscopic responses Y. The comprehensive comparison of the closed-loop reconstruction R^2 scores for both strategies is presented in Figure 14, accompanied by their respective scatter distributions mapped in Figures 15 and 16.

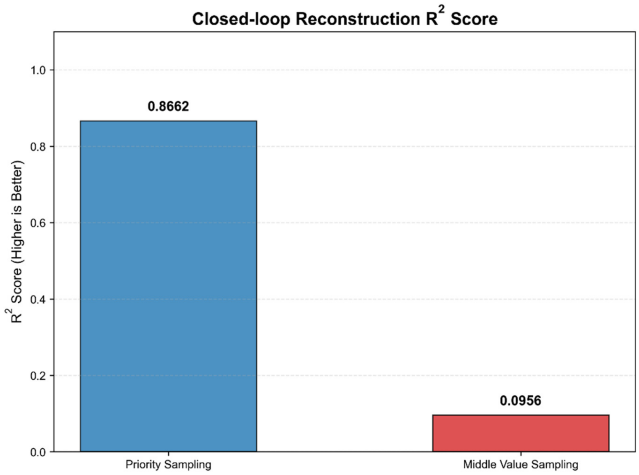


Figure 14. Comparison of closed-loop reconstruction R-squared scores for the two active sampling strategies.

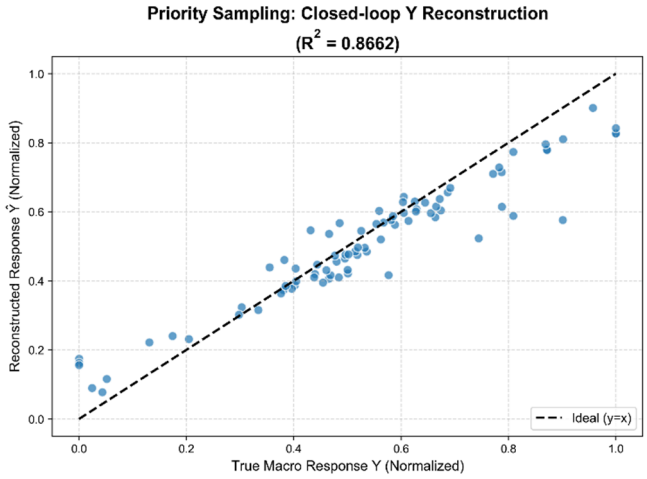


Figure 15. Scatter distribution of actual versus closed-loop reconstructed macroscopic responses for the parameter priority-guided strategy.

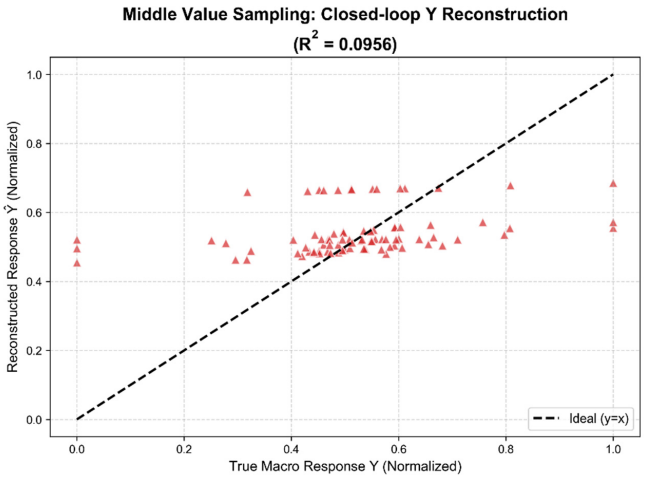


Figure 16. Scatter distribution of actual versus closed-loop reconstructed macroscopic responses for the mid-value specific exploration strategy.

As intuitively reflected in these rigorous comparative evaluations, the inverse model driven by the parameter priority-guided strategy achieves an exceptional closed-loop reconstruction R^2 score of 0.8662. Its corresponding scatter points densely and consistently

wrap around the ideal target diagonal (Figure 16). This validates that the priority sampling mechanism successfully preserves the underlying physical causality, thereby enabling the inverse network to accurately derive reliable parameter combinations capable of satisfying the targeted macroscopic dynamic requirements. Conversely, the mid-value exploration strategy experiences a complete breakdown during this closed-loop validation, yielding a negligible R^2 score of 0.0956. The scatter distribution generated by its reconstructed responses completely degenerates into a scattered horizontal band (Figure 16). This definitive failure proves that the severely biased, center-heavy sampling data fundamentally deprives the inverse neural network of the critical, full-scale boundary information required for generalized physical reconstruction. These final closed-loop verification results decisively prove the superiority of the proposed physics-informed active learning framework, establishing it as a highly reliable tool for both forward dynamic prediction and robust inverse parameter identification in complex concrete numerical models.

5. Conclusions

This study successfully developed and implemented a highly efficient, data-driven active learning framework to overcome the computational bottlenecks and high-dimensional challenges traditionally associated with calibrating the dynamic discrete element parameters of multiphase concrete. By coupling a high-fidelity FDM-DEM numerical approach with an enhanced multi-layer perceptron surrogate model, the complex non-linear mapping between mesoscopic contact parameters and macroscopic dynamic compressive responses under various impact strain rates was rigorously established. As a crucial preparatory step, the Plackett–Burman experimental design was applied to effectively reduce the high-dimensional parameter space from sixteen to eight core variables. This critical dimensionality reduction successfully isolated the most influential factors (accounting for approximately 88% of the total systemic variance) governing the dynamic failure behavior, thereby streamlining the optimization space for the subsequent machine learning pipeline.

The integration of the active learning framework fundamentally transformed the calibration workflow by intelligently querying only the most informative parameter combinations. With an extremely limited computational budget of just 80 actively queried high-fidelity physical simulations, the framework drastically reduced the reliance on massive, computationally expensive static datasets. A systematic comparative analysis revealed that the parameter priority-guided strategy significantly outperformed the mid-value specific exploration strategy. By embedding physical mechanism constraints into the active sampling distribution, the priority-guided approach achieved highly synchronized convergence, stabilizing the training MSE at a low 0.0048 and validation MAE at 0.1054. Rigorous testing confirmed its exceptional forward predictive fidelity, achieving coefficients of determination (R^2) exceeding 0.9 for key macroscopic indicators (specifically Y1 = 0.920, Y2 = 0.911, Y4 = 0.904, and Y6 = 0.926), in stark contrast to the catastrophic predictive failure ($R^2 < 0$) of the mid-value strategy.

Ultimately, leveraging this highly accurate forward mapping, a robust inverse prediction mechanism is successfully constructed for the direct and precise derivation of mesoscopic parameters from targeted macroscopic dynamic responses. Closed-loop validation proves explicitly the superiority of the physics-informed approach explicitly, achieves an exceptional reconstruction R^2 score of 0.8662, and overwhelmingly surpasses the negligible 0.0956 achieved by the center-heavy sampling strategy. While the current physical validations center predominantly around a representative high-impact strain rate to ensure that dynamic failure mechanisms are fully activated, the proposed physics-informed active learning methodology provides a highly reliable, data-efficient, and automated pathway for calibrating complex particulate systems. By seamlessly bridging the gap between

macroscopic performance and mesoscopic mechanisms, this framework offers substantial potential for advancing the numerical investigation and structural design of concrete composites, with multi-strain-rate extensions planned as a necessary future focus.

Despite the promising results achieved by the proposed framework, it is important to acknowledge certain assumptions and limitations inherent in the adopted model. First, regarding the geometric modeling, the concrete aggregates are simplified as convex polyhedra to manage computational complexity. In reality, aggregates possess more irregular morphological features, such as concave surfaces and complex textures, which could further influence the internal interlocking mechanisms and local stress distributions within the ITZ. Second, during the parameter calibration process, a decoupling strategy is employed to reduce the dimensionality of the optimization space by separating the parameters into a static elastic group and a dynamic strength group. While this sequential calibration approach significantly alleviates the computational burden and effectively captures the primary dynamic responses, it inherently neglects the potential minor coupled interactions between static stiffness and dynamic damage evolution, which may introduce a marginal degree of predictive error. Future studies will focus on incorporating more realistic aggregate morphologies and exploring fully coupled high-dimensional optimization algorithms to further refine the calibration accuracy.

Author Contributions: Conceptualization, J.H., Z.L. and T.Z.; methodology, J.H., Z.L. and T.Z.; software, J.H.; formal analysis, J.H.; investigation, J.H. and T.Z.; resources, T.Z.; data curation, J.H.; writing—original draft preparation, J.H.; writing—review and editing, Z.L. and T.Z.; visualization, J.H.; supervision, T.Z.; funding acquisition, T.Z. All authors have read and agreed to the published version of the manuscript.

Funding: This work was supported by the Natural Science Foundation of Shanxi Province (202503021211003).

Data Availability Statement: The original contributions presented in this study are included in the article. Further inquiries can be directed to the corresponding author.

Conflicts of Interest: The authors declare no conflict of interest.

References

1. Chen, Z.; Luo, Q.; Jin, D.; Wang, Z. Numerical study of fractal analysis of crack propagation in concrete under different strain rates by meso-scale particle element modeling. *Int. J. Impact Eng.* **2023**, *173*, 104440. [CrossRef]
2. Zhou, X.; Xie, Y.; Long, G.; Zeng, X.; Li, N.; Ma, G.; Wang, F.; Yao, L. Multi-scale modeling of the concrete SHPB test based on DEM-FDM coupling method. *Constr. Build. Mater.* **2022**, *356*, 129157. [CrossRef]
3. Nitka, M. Static and dynamic concrete calculations: Breakable aggregates in DEM model. *J. Build. Eng.* **2024**, *89*, 109006. [CrossRef]
4. Wu, Y.; Li, Z.; Li, H.; He, M.; Gao, W.; Zhou, J.; Xu, Z. Dynamic response of concrete materials at high strain rates: Experimental and numerical studies. *Eng. Fract. Mech.* **2025**, *330*, 111606. [CrossRef]
5. Asadi, P.; Fakhimi, A. Bonded particle modeling of grain size effect on tensile and compressive strengths of rock under static and dynamic loading. *Adv. Powder Technol.* **2023**, *34*, 104013. [CrossRef]
6. Wu, Z.; Zhang, J.; Fang, Q.; Yu, H.; Haiyan, M. Mesoscopic modelling of concrete material under static and dynamic loadings: A review. *Constr. Build. Mater.* **2021**, *278*, 122419. [CrossRef]
7. Coetzee, C.J. Calibration of the discrete element method. *Powder Technol.* **2017**, *310*, 104–142. [CrossRef]
8. Mohajeri, M.J.; van Rhee, C.; Schott, D.L. Replicating cohesive and stress-history-dependent behavior of bulk solids: Feasibility and definiteness in DEM calibration procedure. *Adv. Powder Technol.* **2021**, *32*, 1532–1548. [CrossRef]
9. Liu, K.; Chen, Z.; Tao, Q.; Wu, D.; Wu, Q.; Zou, P.; Wang, M.; Li, Y. Dynamic mechanical properties and damage morphology analysis of concrete with different aggregates based on FDM-DEM coupling. *Materials* **2024**, *17*, 5804. [CrossRef]
10. Zheng, Y.R.; Feng, X.T.; Cong, Y. Study of correlation between macro and meso mechanical parameters of parallel bonded model. *Rock Soil Mech.* **2018**, *39*, 1289–1301.
11. Potyondy, D.O.; Cundall, P.A. A bonded-particle model for rock. *Int. J. Rock Mech. Min. Sci.* **2004**, *41*, 1329–1364. [CrossRef]

12. Yang, B.; Jiao, Y.; Lei, S. A study on the effects of microparameters on macroproperties for specimens created by bonded particles. *Eng. Comput.* **2006**, *23*, 607–631. [CrossRef]
13. Qin, C.; Zhang, C. Numerical study of dynamic behavior of concrete by meso-scale particle element modeling. *Int. J. Impact Eng.* **2011**, *38*, 1011–1021. [CrossRef]
14. Hanley, K.J.; O'Sullivan, C.; Oliveira, J.C.; Cronin, K.; Byrne, E.P. Application of Taguchi methods to DEM calibration of bonded agglomerates. *Powder Technol.* **2011**, *210*, 230–240. [CrossRef]
15. Yoon, J. Application of experimental design and optimization to PFC model calibration in uniaxial compression simulation. *Int. J. Rock Mech. Min. Sci.* **2007**, *44*, 871–889. [CrossRef]
16. Liu, X.; Wang, Q.; Wang, Y.; Dong, Q. A review of calibration strategies for microscopic parameters in discrete element method. *Powder Technol.* **2023**, *413*, 118042.
17. Benvenuti, L.; Kloss, C.; Pirker, S. Identification of DEM simulation parameters by Artificial Neural Networks and bulk experiments. *Powder Technol.* **2016**, *291*, 456–465. [CrossRef]
18. Derakhshani, S.M.; Schott, D.L.; Lodewijks, G. Micro–macro properties of quartz sand: Experimental investigation and DEM simulation. *Powder Technol.* **2015**, *269*, 127–138. [CrossRef]
19. Ye, F.; Wheeler, C.; Chen, B.; Hu, J.; Chen, K.; Chen, W. Calibration and verification of DEM parameters for dynamic particle flow conditions using a backpropagation neural network. *Adv. Powder Technol.* **2019**, *30*, 292–301. [CrossRef]
20. Choe, J.; Jon, S.; Ryang, W.; Yun, Y.; So, J. Research of laser ultrasonic defect statistics recognition technology based on radial basis function neural network. *Opt. Laser Technol.* **2022**, *150*, 107857. [CrossRef]
21. Hua, L.; Zhang, J.; Li, D.; Xi, X. Fractional gradient descent RBFNN for active fault-tolerant control of plant protection UAVs. *Comput. Model Eng. Sci.* **2024**, *138*, 2129–2157. [CrossRef]
22. Xu, C.; Liu, X.; Wang, E.; Wang, S. Calibration of the microparameters of rock specimens by using various machine learning algorithms. *Int. J. Geomech.* **2021**, *21*, 04021060. [CrossRef]
23. Wang, Y.; Shi, Y.; Yang, T.Y. Structural Performance Warning Based on Computer Intelligent Monitoring and Fractional-Order Multi-Rate Kalman Fusion Method. *Fractal Fract.* **2026**, *10*, 186. [CrossRef]
24. Bolón-Canedo, V.; Remeseiro, B. Feature selection in image analysis: A survey. *Artif. Intell. Rev.* **2020**, *53*, 2905–2931. [CrossRef]
25. Kabir, H.; Garg, N. Machine learning enabled orthogonal camera goniometry for accurate and robust contact angle measurements. *Sci. Rep.* **2023**, *13*, 1497. [CrossRef]
26. Wu, M.F.; Li, C.; Yao, Z.H. Deep active learning for computer vision tasks: Methodologies, applications, and challenges. *Appl. Sci.* **2022**, *12*, 8103. [CrossRef]
27. Ren, P.; Xiao, Y.; Chang, X.; Huang, P.Y.; Li, Z.; Gupta, B.B.; Chen, X.; Wang, X. A survey of deep active learning. *ACM Comput. Surv.* **2022**, *54*, 1–40. [CrossRef]
28. Vaz de Carvalho, C.; Reses, G. Active learning spaces design and assessment: A qualitative systematic literature review. *Interact. Learn. Environ.* **2022**, *30*, 1825–1837.
29. Wang, H.; Geng, H.; Yuan, J.; Zhang, W.; Sheng, H.; Wang, Q.; Li, X. XGBoost-based active learning for wildfire risk prediction. *Comput. Model Eng. Sci.* **2025**, *145*, 3701–3721. [CrossRef]
30. Lv, T.H.; Chen, X.W.; Deng, Y.J.; Chen, G. Further numerical investigation on concrete dynamic behaviors with considering stress non-equilibrium in SHPB test based on the waveform features. *Acta Mech. Sin.* **2020**, *36*, 873–886. [CrossRef]
31. Wittmann, F.H.; Roelfstra, P.E.; Sadouki, H. Simulation and analysis of composite structures. *Mater. Sci. Eng.* **1985**, *68*, 239–248. [CrossRef]
32. Plackett, R.L.; Burman, J.P. The design of optimum multifactorial experiments. *Biometrika* **1946**, *33*, 305–325. [CrossRef]
33. Nitka, M.; Tejchman, J. Effects of aggregate crushing and strain rate on fracture in compressive concrete with a DEM-based breakage model. *Granul. Matter.* **2025**, *27*, 8. [CrossRef]
34. Liu, H.; Yan, Z.; Bian, W.; Wang, F.; Yang, Y.; Zhang, J.; Zhang, P. Exploring the dynamic mechanical properties of self-compacting concrete with recycled asphalt pavement through FDM and DEM coupling approach. *Mater Struct.* **2025**, *58*, 178. [CrossRef]
35. Qu, T.; Feng, Y.T.; Zhao, T.; Wang, M. Calibration of linear contact stiffnesses in discrete element models using a hybrid analytical-computational framework. *Powder Technol.* **2019**, *356*, 795–807. [CrossRef]
36. Qu, T.; Feng, Y.; Zhao, T.; Wang, M. A hybrid calibration approach to Hertz-type contact parameters for discrete element models. *Int. J. Numer. Anal. Methods Geomech.* **2020**, *44*, 1281–1300. [CrossRef]
37. Qu, T.; Feng, Y.T.; Zhao, J. A strain energy-based elastic parameter calibration method for lattice/bonded particle modelling of solid materials. *Powder Technol.* **2022**, *410*, 117860. [CrossRef]

Disclaimer/Publisher's Note: The statements, opinions and data contained in all publications are solely those of the individual author(s) and contributor(s) and not of MDPI and/or the editor(s). MDPI and/or the editor(s) disclaim responsibility for any injury to people or property resulting from any ideas, methods, instructions or products referred to in the content.